Geomechanics and Engineering, *Vol. 42, No. 4 (2025) 281-297*
https://doi.org/10.12989/gae.2025.42.4.281

Numerical study on dry and immersed granular collapse: Role of particle shape and initial particle orientation

Lei Jin*[1], Wenjie Xu[2] and Jingjing Li[1]

[1]*College of Civil Engineering, Jiangsu Open University, Jiangsu, China*
[2]*State Key Laboratory of Hydroscience and Engineering, Tsinghua University, Beijing, China*

(*Received January 25, 2025, Revised July 29, 2025, Accepted July 30, 2025*)

Abstract. The shape of natural rock and soil particles is distinct and their orientation may prefer a certain direction, and determining the influences of particle shape and initial particle orientation on dry and immersed granular collapse is of great significance to prevention of geological disasters such as subaerial and submarine landslides. Using the superquadric DEM and the coupled CFD-DEM, the dry and immersed collapse process of granular columns with different particle shapes (aspect ratio A and blockiness B) and different initial particle orientations θ are simulated. The results show that, compared with the case of A = 1 (spherical), the collapse of particles with larger A (elongated) or smaller A (platy) results in a shorter final runout distance and a higher final deposit height. The collapse of particles with larger B (more angular) also results in a shorter final runout distance and a higher final deposit height. The collapse of particles with $\theta = 0°$ (approximately horizontal) produces an obviously smaller final runout distance, and progresses in a particular way that some particles being first squeezed out from the lateral free surface followed by the gradual slide of particles in the upper parts. For platy ellipsoidal particles, the collapse of particles with $\theta = 135°$ (leaning on the fixed wall) generates the longest final runout distance. Whereas, for elongated ellipsoidal particles, the collapse of particles with $\theta = 90°$ (approximately upright) generates the longest final runout distance.

Keywords: CFD-DEM; dry granular collapse; immersed granular collapse; initial particle orientation; particle shape; superquadric

1. Introduction

Granular flows result from landslides and rock avalanches often occur in mountain and canyon areas on land, often with strong impact force and extensive runout, which can damage nearby buildings, transportation facilities and hydropower stations, and even cause impulse waves and dam break (Xing *et al.* 2025, Chen *et al.* 2024). Besides, submarine landslides are also destructive geological disasters, which can damage offshore oil and gas drilling platforms, submarine communication cables and pipelines, and even further cause giant tsunamis (Zhang *et al.* 2021, Guo *et al.* 2023). The occurrence of these geological disasters is mostly manifested as the collapse, spread and deposit of rock and soil particles, which is a very complex dynamic process. The collapse of a granular column on a horizontal or an inclined plane is a commonly employed small-scale model for understanding the underlying physical mechanisms and predicting the consequences of these disasters (Lube *et al.* 2005, Trepanier and Franklin 2010, Rondon *et al.* 2011, Bougouin *et al.* 2019, Zhang *et al.* 2024).

In recent years, with the great improvement of computer computing power and the rapid development of numerical algorithms, the simulations of subaerial and submarine landslides have attracted much attention in the fields of geomechanics and engineering. In general, the dry granular collapse in air is used to simulate subaerial landslides, and only solid particles are considered without the influence of ambient air. The immersed granular collapse in water is used to simulate submarine landslides, and the influence of ambient water should be considered. The commonly used numerical simulation methods for dry granular collapse can be divided into two categories, namely the continuum-based numerical method and discrete element method (DEM). The former mainly includes the finite element method (FEM), particle finite element method (PFEM), smoothed particle hydrodynamics (SPH) and material point method (MPM) (Crosta *et al.* 2009, Zhang *et al.* 2015, Kermani and Qiu 2020, Fan *et al.* 2024). The DEM can directly consider the discrete essence of natural rock and soil mass and deepen our insights into the internal microstructure, and thus it is widely used for analyzing the granular collapse dynamics (Tapia-McClung and Zenit 2012, Kermani *et al.* 2015, Cui *et al.* 2021, Lai *et al.* 2023, Hoang and Nguyen 2023, Gong *et al.* 2024). To further simulate the fluid flow and the interaction between fluids and particles during the immersed granular collapse, it is necessary to introduce some pertinent numerical methods for fluid flow and realize the coupling with the DEM. Among these are the conventional computational fluid dynamics (CFD), lattice Boltzmann method (LBM) and SPH, and the CFD mainly includes finite volume method (FVM) and FEM (Jing *et al.* 2018, Sun *et al.* 2020, Polanía *et al.* 2022, Bao *et al.* 2023, Coppin *et al.* 2023, Kumar *et al.* 2017, Yang *et al.* 2019, Xu

---

*Corresponding author, Ph.D.
E-mail: jinl@jsou.edu.cn

ISSN: 2005-307X (Print), 2092-6219 (Online)

et al. 2019). Due to the lower computational cost and reasonable simulation accuracy in general geotechnical engineering problems, the unresolved CFD-DEM coupling algorithm has been applied to simulate the immersed or wet granular collapse by several researchers, but most of them adopted spherical solid particles (Jing *et al.* 2018, Sun *et al.* 2020, Polanía *et al.* 2022).

It is well-known that, due to various geological origins, particles in natural rock and soil masses possess distinct shapes and their orientations may prefer a certain direction, both of which have a great impact on the strength and deformation properties of rock and soil masses (Gong *et al.* 2021, Adesina *et al.* 2024, Fu and Dafalias 2011, Dong *et al.* 2022). Several scholars have also tried to explore the influence of particle shape and particle orientation on the collapse characteristics of granular columns. In terms of dry granular collapse, Lube (2005) and Trepanier (2010), based on the results of laboratory physical model tests, argued that the particle shape has little influence on granular collapse. Tapia-McClung and Zenit (2012) performed DEM simulations with elongated particles composed of multiple spheres, and also suggested that the particle shape has little impact on the granular collapse. Cui *et al.* (2021) conducted DEM simulations with random polyhedral particles, and noted that, with the decrease of particle aspect ratio, the final deposit height decreases and the final runout distance increases. Hoang and Nguyen (2023) conducted DEM simulations with superquadric particles, and claimed that the particle blockiness and the particle aspect ratio both have an important impact on the granular collapse and the relationship between the final runout distance and the particle aspect ratio is not monotonous. The study of Gong *et al.* (2024), based on the well-known commercial DEM software PFC, reported that the particle sphericity and angularity have an important effect on deposition morphology, while the roughness has a weaker influence. In terms of immersed granular collapse, Bao *et al.* (2023) carried out numerical simulations using the coupled CFD-DEM with random polyhedral particles and analyzed the influences of particle sphericity, angularity, and roughness on the granular collapse characteristics. Approximating elongated particles by combining several disks, Coppin *et al.* (2023) conducted 2D simulations using the coupled FEM-DEM and analyzed the influence of different initial particle orientations.

To sum up, the conclusions of previous studies are still controversial as for the particle shape effects on the dry granular collapse, and very little research focuses on the particle shape effects on the immersed granular collapse. Besides, the influences of initial particle orientation on dry and immersed granular collapse are both rarely reported. On the other hand, the non-spherical particles used in previous DEM simulations are mainly described by multi-sphere model and random polyhedron model. In fact, the superquadric DEM developed in recent years provides another alternative, as superquadrics allow non-spherical shapes to be accurately described by varying shape parameters, namely particle aspect ratio and blockiness, which make it easier to specifically study the role of particle shape and particle orientation (Hoang and Nguyen 2023, Soltanbeigi *et al.* 2018, Zhao *et al.* 2019, Gao *et al.* 2022, Wedel *et al.* 2024). To this end, this study attempts to simulate the dry and immersed granular collapse process based on the superquadric DEM and the coupled CFD-DEM, with an emphasis on investigating the effects of different particle shapes and initial particle orientations on collapse characteristics and gaining an insight into the underlying physical mechanisms.

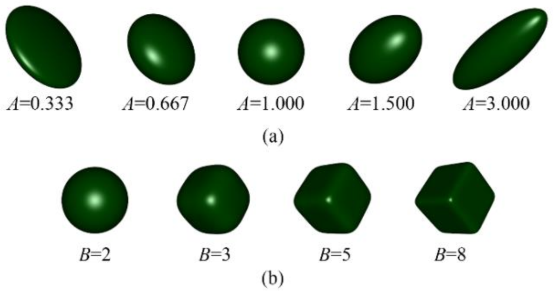

Fig. 1 Superquadric models of particles with different shapes: (a) B = 2 and (b) A = 1

2. Numerical formulations

2.1 Solid phase (Superquadric DEM)

In the superquadric DEM (Hoang and Nguyen 2023, Soltanbeigi *et al.* 2018, Zhao *et al.* 2019, Gao *et al.* 2022, Wedel *et al.* 2024), the surface morphology of a non-spherical particle can be defined by the following equation

$$F(x,y,z)=\left[\left(\frac{x}{a}\right)^m+\left(\frac{y}{b}\right)^m\right]^{\frac{n}{m}}+\left(\frac{z}{c}\right)^n-1=0 \tag{1}$$

where a, b, c are the three semi-major axes lengths and m, n are blockiness parameters that control the sharpness of the surface edges. When m = n = 2, a sphere or ellipsoid can be generated. When m = 2 and $n \gg 2$, an approximate cylinder can be generated. When $m \gg 2$ and $n \gg 2$, an approximate cube or cuboid can be generated. In the following, particle shapes are described by aspect ratio A and blockiness B, which are respectively defined as $A = c/a = c/b$ and B=m=n. In this study, several typical particle shapes shown in Fig. 1 are selected for simulations of granular collapse.

The translational and rotational motion of a particle i can be expressed by Newton's second law as follows

$$m_i\frac{\mathrm{d}\boldsymbol{u}_{\mathrm{p},i}}{dt}=\sum_{j=1}^{n_i^{\mathrm{c}}}\boldsymbol{F}_{ij}^{\mathrm{c}}+\boldsymbol{F}_i^{\mathrm{f}}+m_i\boldsymbol{g} \tag{2}$$

$$I_i\frac{\mathrm{d}\boldsymbol{\omega}_i}{dt}=\sum_{j=1}^{n_i^{\mathrm{c}}}\boldsymbol{M}_{ij}^{\mathrm{c}} \tag{3}$$

where m_i and I_i are respectively the particle mass and moment of inertia, $\boldsymbol{u}_{\mathrm{p},i}$ and $\boldsymbol{\omega}_i$ respectively the translational velocity and angular velocity, $\boldsymbol{F}_{ij}^{\mathrm{c}}$ and $\boldsymbol{M}_{ij}^{\mathrm{c}}$ respectively the contact force and moment acting on particle *i* due to contacting with neighbor particle or wall *j*, *t* the time, n_i^{c} the total contact number of particle *i* with neighbor particles and walls, $\boldsymbol{g}$ the gravitational acceleration, and $\boldsymbol{F}_i^{\mathrm{f}}$ the force acting on particle *i* due to interacting with the fluid phase, including buoyancy force and drag force.

Compared with spherical particles, the non-spherical nature of superquadric particles makes contact detection between them more complex and time-consuming, and a "broad to narrow" two-phase contact detection algorithm can be employed to improve the computational efficiency. In the first broad phase, a potential contact between two particles is found by successively judging whether the corresponding bounding spheres and oriented bounding boxes (OBB, these boxes are large enough to encompass the entire particle and are aligned with the orientation of the three main axes of the particle) are in contact. In the second narrow phase, the deepest point method solved by a Lagrangian multiplier algorithm is employed to find the maximum penetration/minimum distance between a detected potential contact pair.

After contact detection, if particle *i* and particle *j* are in contact, the normal contact force $\boldsymbol{F}_{\mathrm{n},ij}$ and tangential contact force $\boldsymbol{F}_{\mathrm{t},ij}$ can be calculated as follows

$$\boldsymbol{F}_{\mathrm{n},ij} = -k_{\mathrm{n},ij}\boldsymbol{\delta}_{\mathrm{n},ij} - \eta_{\mathrm{n}}\boldsymbol{v}_{\mathrm{n},ij} \tag{4}$$

$$\boldsymbol{F}_{\mathrm{t},ij} = \begin{cases} -k_{\mathrm{t},ij}\boldsymbol{\delta}_{\mathrm{t},ij} - \eta_{\mathrm{t}}\boldsymbol{v}_{\mathrm{t},ij} \ , & \left|\boldsymbol{F}_{\mathrm{t},ij}\right| \le \mu\left|\boldsymbol{F}_{\mathrm{n},ij}\right| \\ -\mu\left|\boldsymbol{F}_{\mathrm{n},ij}\right|\boldsymbol{t}_{ij} \ , & \left|\boldsymbol{F}_{\mathrm{t},ij}\right| > \mu\left|\boldsymbol{F}_{\mathrm{n},ij}\right| \end{cases} \tag{5}$$

where $k_{\mathrm{n},ij}$ and $k_{\mathrm{t},ij}$ denote respectively the normal and tangential contact stiffness, $\boldsymbol{\delta}_{\mathrm{n},ij}$ and $\boldsymbol{\delta}_{\mathrm{t},ij}$ respectively the normal and tangential relative displacement of the contact, $\boldsymbol{v}_{\mathrm{n},ij}$ and $\boldsymbol{v}_{\mathrm{t},ij}$ respectively the normal and tangential relative velocity of the contact, μ the friction coefficient of the contact, and $\boldsymbol{t}_{ij}$ the unit tangential vector of the contact. Moreover, η_{n} and η_{t} are respectively the normal and tangential damping coefficients of the contact, which can be calculated from the restitution coefficient of particle collision.

The Hertzian model is used to calculate the normal and tangential contact stiffnesses as follows

$$k_{\mathrm{n},ij} = \frac{4}{3}\frac{E_i E_j\sqrt{R_{ij}^*}}{E_i(1-\nu_j^{\,2}) + E_j(1-\nu_i^{\,2})}\sqrt{\boldsymbol{\delta}_{\mathrm{n},ij}} \tag{6}$$

$$k_{\mathrm{t},ij} = \frac{8G_i G_j\sqrt{R_{ij}^*}}{G_i(1-\nu_j^{\,2}) + G_j(1-\nu_i^{\,2})}\sqrt{\boldsymbol{\delta}_{\mathrm{n},ij}} \tag{7}$$

Where E_i and E_j are respectively the Young's modulus for the particles *i* and *j*, ν_i and ν_j respectively the Poisson's ratio of the particles *i* and *j*, and G_i and G_j respectively the shear modulus of the particles *i* and *j*. Moreover, R_{ij}^* is the equivalent radius at the contacting point, which is formulated as $R_{ij}^* = R_i R_j/(R_i + R_j)$. R_i and R_j denote the equivalent radius of the curvature at the deepest point, that is, the reciprocal of the average curvature K, which can be calculated as

$$K = \frac{1}{2\left|\nabla F\right|^3}\left[\nabla F^{\mathrm{T}}\cdot\nabla^2 F\cdot\nabla F - \left|\nabla F\right|^2\Delta F\right] \tag{8}$$

where ∇F, $\nabla^2 F$ and ΔF are the first derivative (gradient vector), second derivative (Hessian matrix) and Laplace operator of the superquadric function on the left of Eq. (1), respectively.

2.2 Fluid phase (CFD)

In the CFD, the fluid phase is governed by the modified Navier-Stokes equations for the presence of particles, that is, the volume-averaged equations, which are solved via the finite volume method in the Eulerian framework. In particular, the mass and momentum conservation equations are expressed in vector form as follows

$$\frac{\partial(\alpha_{\mathrm{f}}\rho_{\mathrm{f}})}{\partial t} + \nabla\cdot(\alpha_{\mathrm{f}}\rho_{\mathrm{f}}\boldsymbol{u}_{\mathrm{f}}) = 0 \tag{9}$$

$$\begin{aligned} &\frac{\partial(\alpha_{\mathrm{f}}\rho_{\mathrm{f}}\boldsymbol{u}_{\mathrm{f}})}{\partial t} + \nabla\cdot(\alpha_{\mathrm{f}}\rho_{\mathrm{f}}\boldsymbol{u}_{\mathrm{f}}\boldsymbol{u}_{\mathrm{f}}) = \\ &\qquad -\alpha_{\mathrm{f}}\nabla p + \alpha_{\mathrm{f}}\nabla\cdot\boldsymbol{\tau}_{\mathrm{f}} + \alpha_{\mathrm{f}}\rho_{\mathrm{f}}\boldsymbol{g} - \boldsymbol{F}_{\mathrm{f,s}} \end{aligned} \tag{10}$$

where α_{f} is the fluid volume fraction (porosity) of a fluid cell, ρ_{f} the fluid density, $\boldsymbol{u}_{\mathrm{f}}$ the volume-averaged fluid velocity, p the fluid pressure, and $\boldsymbol{F}_{\mathrm{f,s}}$ the interaction force between fluid and particles. Moreover, $\boldsymbol{\tau}_{\mathrm{f}}$ is the viscous stress tensor of the fluid, which can be formulated as $\boldsymbol{\tau}_{\mathrm{f}} = \mu_{\mathrm{f}}[\nabla\boldsymbol{u}_{\mathrm{f}} + (\nabla\boldsymbol{u}_{\mathrm{f}})^T]$ for Newtonian fluids, and μ_{f} is the dynamic viscosity of the fluid.

2.3 Fluid-particle interaction (CFD-DEM)

A key step to realize the coupling of CFD and superquadric DEM is how to capture the fluid-particle interaction, particularly how to calculate the fluid drag force on non-spherical superquadric particles. A number of physical tests have been carried out on the settling of a single non-spherical particle in water in previous studies, and several drag coefficient models have been proposed (Ganser 1993, Hözer and Sommerfeld 2008, Wang *et al.* 2018). In terms of the commonly used Hölzer-Sommerfeld model (Hözer and Sommerfeld 2008), the drag coefficient can be formulated as follows

$$\begin{aligned} C_{\mathrm{D0}} = {} & \frac{8}{Re_{\mathrm{p}}}\frac{1}{\sqrt{\varphi_{\perp}}} + \frac{16}{Re_{\mathrm{p}}}\frac{1}{\sqrt{\varphi}} + \frac{3}{\sqrt{Re_{\mathrm{p}}}}\frac{1}{\varphi^{3/4}} \\ & + 0.42\times10^{0.4(-\log(\varphi))^{0.2}}\frac{1}{\varphi_{\perp}} \end{aligned} \tag{11}$$

where Re_{p} is the particle Reynolds number. φ denotes the particle sphericity, which is the ratio between the surface area of a volume equivalent sphere (a sphere with a volume equal to that of the non-spherical particle) and the surface area of the non-spherical particle. Moreover, $\varphi_\perp$ labels the crosswise sphericity, which is the ratio between the central cross-sectional area of a volume equivalent sphere and the projected cross-sectional area of the non-spherical particle perpendicular to the flow direction.

Further, Di Felice model (DIFELICE 1994) can be employed to correct the drag coefficient of a single particle obtained via Eq. (11) to consider the influence of surrounding particles, which is written as follows

$$\beta_i = \frac{3}{4}\frac{\alpha_\mathrm{f}(1-\alpha_\mathrm{f})\rho_\mathrm{f}\left|\boldsymbol{u}_{\mathrm{f},i}-\boldsymbol{u}_{\mathrm{p},i}\right|}{d_{\mathrm{V},i}}C_{\mathrm{D0}}{\alpha_\mathrm{f}}^{1-\chi} \tag{12}$$

$$\chi = 3.7 - 0.65\exp[-\frac{(1.5-\log Re_\mathrm{p})^2}{2}] \tag{13}$$

where $d_{\mathrm{V},i}$ is the diameter of the volume equivalent sphere of particle i, and $\boldsymbol{u}_{\mathrm{f},i}$ is the fluid velocity at the mass center of particle i. Then, the fluid drag force acting on the particle i can be calculated as

$$F_{\mathrm{d},i} = \frac{\beta_i V_i(\boldsymbol{u}_{\mathrm{f},i}-\boldsymbol{u}_{\mathrm{p},i})}{\alpha_\mathrm{f}(1-\alpha_\mathrm{f})} \tag{14}$$

where V_i is the volume of particle i.

It is noteworthy that the aforementioned fluid-particle coupling algorithm neglects the effects of hydrodynamic torque. Similarly, Gao *et al.* (2021) and Bao *et al.* (2023) disregarded hydrodynamic torque in their simulations of irregular particle-fluid interactions, yet reported overall reasonable agreements in their results. Consequently, this study adopts the premise that inter-particle collisions dominate the granular column collapse process, and that neglecting hydrodynamic torque exerts limited influence on the overall collapse dynamics and the final deposit geometry. It should be noted, however, that hydrodynamic torque may exert significant effects for highly anisotropic (e.g., platy or elongated) particles or under high-flow-velocity conditions. Addressing this specific issue would require alternative numerical approaches, such as the cluster-based modeling methods (Coppin *et al.* 2023) or resolved CFD-DEM/LBM-DEM for irregularly particles, which are beyond the scope of the present study.

The aforementioned CFD-DEM coupling formulation belongs to an unresolved volume-averaged algorithm. For general applications, since DEM time step is usually smaller than CFD time step, DEM iterations should be conducted as a sub-cycling in each CFD iteration to maintain synchronous calculation of both solvers. The above numerical algorithms of superquadric DEM and CFD-DEM coupling have been implemented in MFiX 23.2, an open-source software package developed by NETL in the United States, and detailed validations have been performed against multiple benchmark problems. For more details, please refer to the references (Gao *et al.* 2022, Gao *et al.* 2021). On this basis, we attempt to make some improvements and realize the numerical simulations of dry and immersed granular collapse.

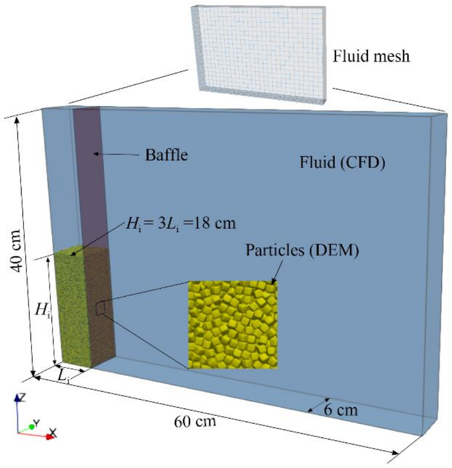

Fig. 2 Initial numerical model for granular collapse (*A*1-*B*5-Water)

3. Model configuration and case plan

This study focuses on the effects of different particle shapes and different initial particle orientations on the dry and immersed granular collapse. Since we do not aim to reproduce the exact details of any laboratory experiments, we choose the model setup and parameters based on general choices in the literature. As shown in Fig. 2, the computational domain is a narrow cuboid region, and the length (x direction), width (y direction) and height (z direction) are 60 cm, 6 cm and 40 cm respectively, with a gravitational acceleration of 9.8 $\mathrm{m\cdot s^{-2}}$ pointing down along the vertical z axis. The surrounding, bottom and top boundaries of the domain are all fixed walls. The initial granular column samples are generated in the left container zone delimited by a baffle located at x = 6 cm. The particle size used in the model is set to 3.17 mm based on a comprehensive consideration of size effects and computational efficiency, and the particle size of a non-spherical particle refers to the diameter of its volume equivalent sphere. A set of typical DEM parameters are selected and listed in Table 1. To increase the DEM time step and reduce the computing cost, the value of Young's modulus is not as large as that of actual rock and soil particles, which is considered to have little influence on the simulation results of granular collapse (Jing *et al*. 2018).

The initial granular columns are prepared via gravitational deposition of particles. In this process, the influence of fluid is not considered and thus only DEM is activated. The specific steps are as follows: (1) Non-overlapping particles are first generated in the left container zone. When considering the influence of different particle shapes, the initial orientation of particles is randomly distributed, while the particles should be set to a specified orientation when considering the influence of different initial orientations; (2) The particles' rotations are locked and then allowed to deposit under gravity until they approach equilibrium state. In this step, the friction coefficient is set to a temporary value of 0.0 to generate a dense sample; (3) After the particles' rotations are released and the friction coefficient is adjusted to 0.5, the model is cycled until an equilibrium state is reached again.

Table 1 Numerical model parameters for the granular collapse

Parameter	Unit	Value
Particle diameter	mm	3.17
Particle density	kg·m^{-3}	2500
Young's modulus of particles	Pa	1.0×10^{7}
Poisson's ratio of particles	-	0.2
Particle-particle friction coefficient	-	0.5
Particle-wall friction coefficient	-	0.5
Particle-particle restitution coefficient		0.5
Particle-wall restitution coefficient		0.5
Fluid density	kg·m^{-3}	1000
Fluid dynamic viscosity	Pa·s	0.001
Fluid cell size	mm	20
DEM time step	s	2.5×10^{-6}
CFD time step	s	5×10^{-5}

In this study, a granular column is generated with an initial length of L_i = 6 cm, width of 6 cm and height of H_i = 18 cm, hence the initial column aspect ratio is $a = H_i / L_i = 3$, as shown in Fig. 2. Then, the baffle is directly deleted to allow the particles collapse onto the horizontal bottom surface under gravity. At this point, in terms of the immersed collapse in water, the CFD-DEM coupling should be activated and the relevant parameters are listed in Table 1. The initial fluid flow velocity is assumed to be zero, and the boundaries are considered to be non-slip. Previous studies indicate that in unresolved CFD-DEM simulations of dense particle-fluid systems, the CFD cell size should generally exceed 2–5 times the particle diameter to ensure accuracy in porosity computation. However, excessively large CFD cell sizes may compromise fluid resolution. In this study, a CFD cell size of 20 mm (approximately six times the particle diameter) is selected to ensure convergence in porosity calculations while maintaining no discernible impact on the overall characteristics of the flow field.

In this study, the numerical simulations are divided into two groups. The first group of simulations focuses on the dry and immersed collapse of granular columns with different particle shapes, and the initial particle orientations are all set as a random distribution. As stated in Sect. 2.1, the particle shape is characterized by the aspect ratio A and blockiness B, and typical cases such as spherical, blocky, platy and elongated particles are adopted in our simulations, as shown in Fig. 1. The particles of the column shown in Fig. 2 are blocky particles with A = 1 and B = 5 (approximately cubes), and it can be seen that the orientations of the particles are initially disordered. The dry and immersed collapse of this granular column are respectively labeled as "A1-B5-Dry" and "A1-B5-Water", and so on for other cases. In the second group of simulations, the dry and immersed collapse of granular columns with different initial particle orientations are explored. The particle orientation is described by the inclination angle θ relative to the positive horizontal direction, which is selected as 0°, 45°, 90° and 135° respectively for both the platy ellipsoidal particle A0.333-B2 and elongated ellipsoidal particle A3.000-B2, as shown in Fig. 3. θ = 0 indicates the particles are placed horizontally, which means the shortest axis is parallel to the vertical z direction for a A0.333-B2 particle and the longest axis parallel to the horizontal x direction for a A3.000-B2 particle, and the other orientation angles can be obtained by rotating the particle of θ = 0 around the y direction. It should be noted that the specified initial particle orientation may be slightly altered in the above sample preparation step (3), as shown in Fig. 3, and thus we can regard θ as the main initial particle orientation.

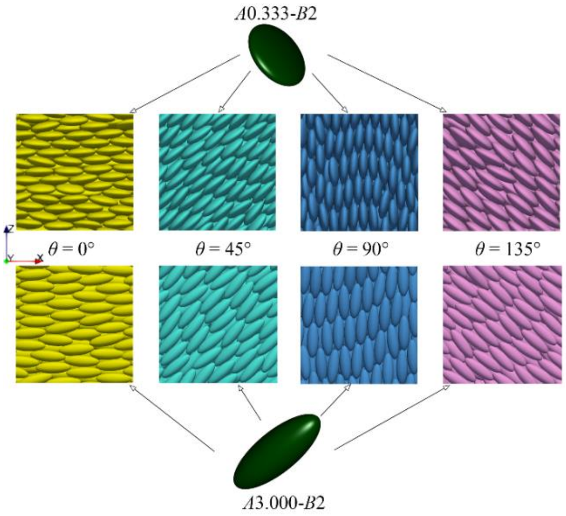

Fig. 3 Zooms on the granular columns with different initial particle orientations

The numerical models comprised approximately 27,000 particles. Parallel computations are performed on a desktop computer featuring an Intel® Core™ i7-13700KF processor (16 cores/24 threads, up to 5.4 GHz boost frequency). Simulation runtime exhibits significant dependence on superquadric particle shape and fluid-particle interaction. The most computationally intensive case A1-B8-Water consumed approximately 8.9 days to complete.

4. The role of particle shape

4.1 Final deposit geometry

The final deposit geometry is commonly characterized by the final runout distance L_f and deposit height H_f, and determining the two indicators is an important issue in the study of granular collapse because they reflect the mobility of particles and are of great value for disaster risk assessment. As shown in Fig. 4, after granular collapse, the maximum deposit height generally appears at the leftmost edge (x = 0), and the lowest stacking height observed in the left view (zy coordinate plane) is regarded as H_f. In the later stage of granular collapse process, some front particles would gradually spread out from the main particle system,

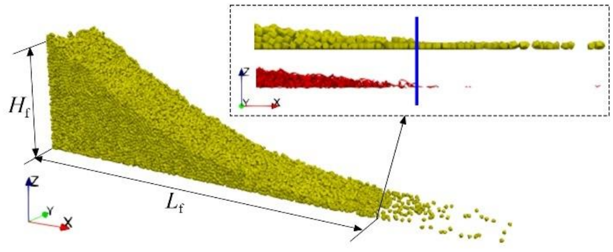

Fig. 4 Final deposit after granular collapse (A1-B5-Dry)

especially in the case of dry collapse, which brings certain difficulties to the reasonable determination of L_f. Bougouin *et al*. (2019) proposed four criteria based on the distribution characteristics of particles at the front. Some other researchers such as Cabrera and Estrada (2019) and Gong *et al.* (2024) took the position where the deposit contact network begins to break off as the farthest runout point. In present study, some of these methods are tested and compared, and it is found that the position of the transition from two layers of particles to one layer observed in the front view (*zx* coordinate plane) is basically the same as the position where the contact network begins to break off (see the blue line in the inset of Fig. 4, the red lines are connection lines between two contacting particles). Therefore, we use these two methods to estimate L_f of the granular collapse.

The variation of the simulated final runout distance and deposit height with the particle aspect ratio and particle blockiness is shown in Fig. 5, where the final runout distance and deposit height are respectively normalized as $[L_f]=(L_f-L_i)/L_i$ and $[H_f]=H_f/H_i$. As can be seen from Fig. 5, whether spherical particles or non-spherical particles, the final runout distance of the immersed granular collapse is significantly reduced compared with the dry case and the final deposit height is slightly increased. Obviously, the presence of ambient water weakens the fluidity of particles, which is consistent with previous results (Jing *et al.* 2018, Bao *et al*. 2023, Coppin *et al*. 2023).

As can be seen from Fig. 5(a), as the particle aspect ratio is changed, the variation patterns of the final runout distance and deposit height are similar for both dry and immersed collapse. Specifically, the final runout distance of the spherical particles is the longest and the deposit height is the lowest. From the turning point $A = 1$ to both sides, the larger A (elongated) or smaller A (platy) is, the final runout distance decreases and deposit height increases gradually. The above simulation results are consistent with those obtained by Cui *et al.* (2021) and Gong *et al.* (2024) for dry granular collapse and Bao *et al*. (2023) for immersed granular collapse, but different from those obtained by Hoang and Nguyen (2023) for dry granular collapse, which reported a complex non-monotonous variation on both sides of $A = 1$.

It can be seen from Fig. 5(b) that the variation patterns of the final runout distance and deposit height with the particle blockiness are also similar for both dry and immersed granular collapse. Specifically, with the increase of blockiness B, the particle evolving from sphere to cube, the final runout distance decreases and the deposit height increases, which is consistent with the results obtained by Hoang and Nguyen (2023). In addition, it can be inferred from Fig. 5 that when the particle shape deviates from the sphere to a large extent, the particle aspect ratio and blockiness both have less effect.

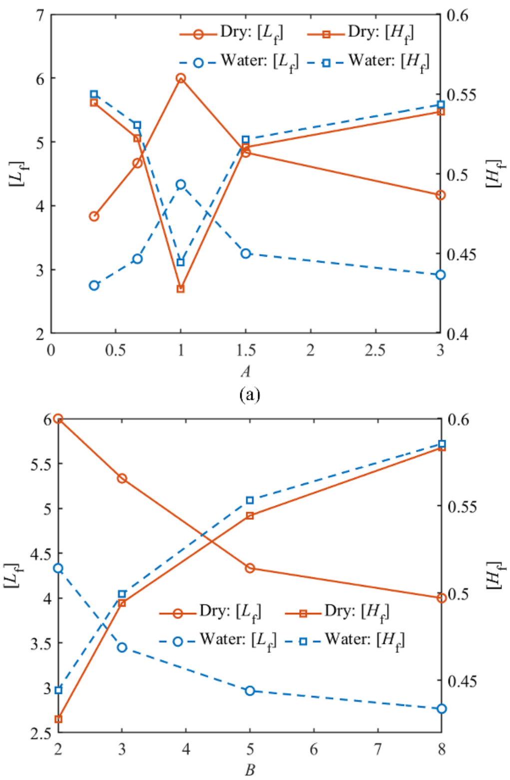

Fig. 5 Variation of final runout distance and deposit height with (a) particle aspect ratio and (b) particle blockiness

4.2 Collapse dynamics

Fig. 6 illustrates the particle translational velocity of *A*1-*B*2 (sphere), *A*0.333-*B*2 (platy ellipsoid), *A*3.000-*B*2 (elongated ellipsoid) and *A*1-*B*5 (approximate cube) at 0.1 s, 0.25 s, 0.5 s and 1.2 s, respectively. In this study, the time of baffle deletion corresponds to $t = 0$ s. Fig. 7 shows the near-field flow field of the case *A*1-*B*5-Water at 0.1 s, 0.25 s, 0.5 s and 1.2 s, respectively. In Fig. 7, the color scale indicates the flow velocity magnitude, and the gray arrow lines represents the flow velocity vector. Moreover, the black curves in the flow field at 0.1 s, 0.25 s, and 0.5 s capture the profile of the moving sliding body, while the black curve in the flow field at 1.2 s delineates the surface of final deposit.

Fig. 8 shows the energy evolution curves during the dry collapse of the cases *A*1-*B*2 and *A*0.333-*B*2, including the normalized particle gravitational potential energy $[E_p]$, particle kinetic energy $[E_{kp}]$ and dissipated energy $[E_d]$. Fig. 9 shows the energy evolution curves during the immersed collapse of the cases *A*1-*B*2 and *A*0.333-*B*2, including the normalized particle gravitational potential

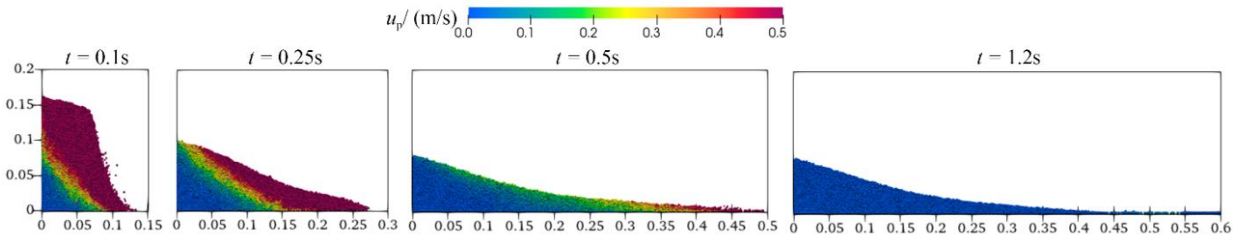

(a) $A1$-$B2$-Dry

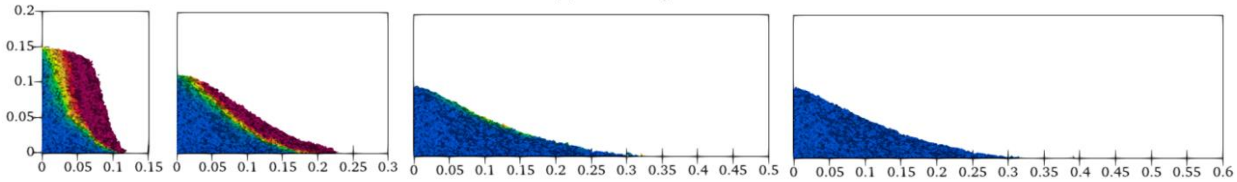

(b) $A0.333$-$B2$-Dry

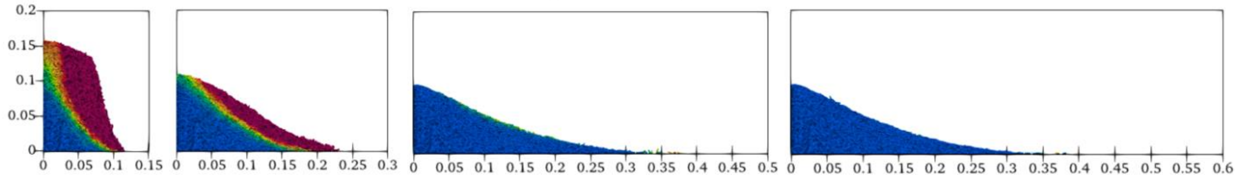

(c) $A3.000$-$B2$-Dry

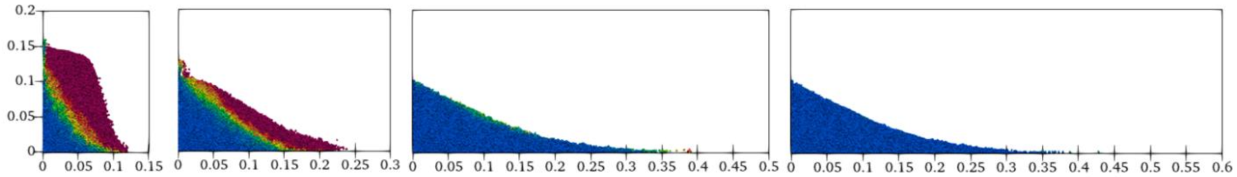

(d) $A1$-$B5$-Dry

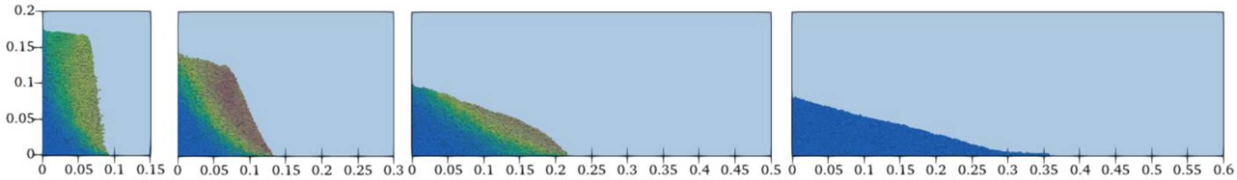

(e) $A1$-$B2$-Water

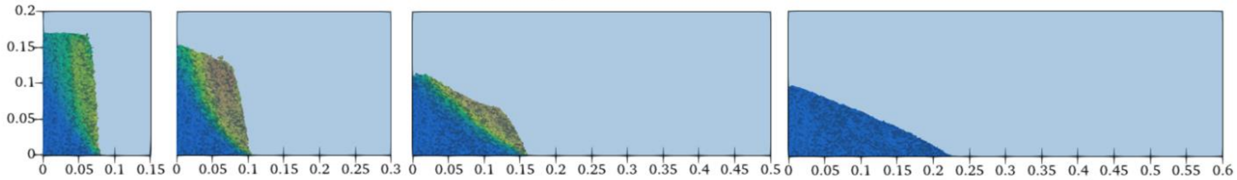

(f) $A0.333$-$B2$-Water

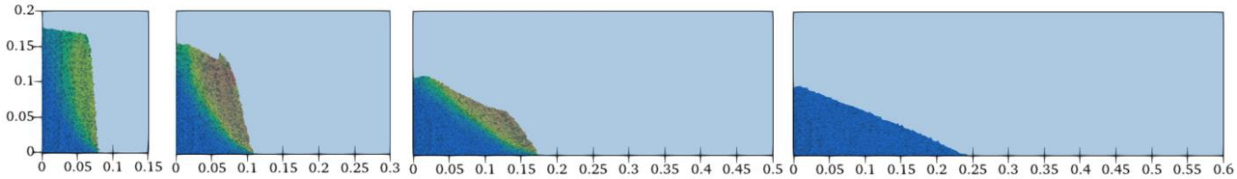

(g) $A3.000$-$B2$-Water

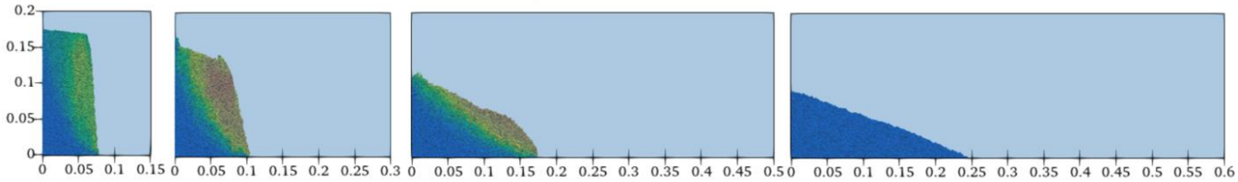

(h) $A1$-$B5$-Water

Fig. 6 Snapshots of the particle translational velocity during granular collapse with different particle shapes (the immersed cases are distinguished by light blue background)

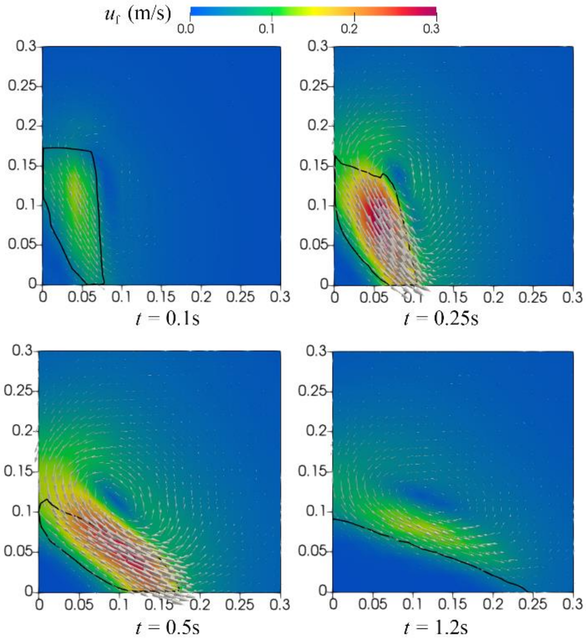

Fig. 7 Snapshots of the near-field flow field during granular collapse of the case $A1$-$B5$-Water

energy $[E_p]$, particle kinetic energy $[E_{kp}]$, fluid kinetic energy $[E_{kf}]$ and dissipated energy $[E_d]$. Moreover, the increments of particle rotational kinetic energy and fluid gravitational potential energy are not involved in the energy calculation due to their negligible effects (Gong *et al*. 2024, Jing *et al*. 2018, Coppin *et al*. 2023). The normalized energies are calculated as follows

$$[E_p]=\frac{\sum_{i=1}^{N_p} m_i g h_i}{E_{p0}} \tag{15}$$

$$[E_{kp}]=\frac{\sum_{i=1}^{N_p} m_i u_{p,i}^2}{2E_{p0}} \tag{16}$$

$$[E_{kf}]=\frac{\rho_f V_f \sum_{n=1}^{N_f} \alpha_{fn} u_{fn}^2}{2E_{p0}} \tag{17}$$

$$[E_d]=1-[E_p]-[E_{kp}]-[E_{kf}] \tag{18}$$

where E_{p0} denotes the particle gravitational potential energy of the initial granular column, N_p the total number of particles, h_i the height of the center of mass of particle i, N_f the total number of fluid cells in the immersed models, V_f the volume of each fluid cell, α_{fn} the fluid volume fraction (porosity) of fluid cell n, and u_{fn} the fluid velocity magnitude of fluid cell n.

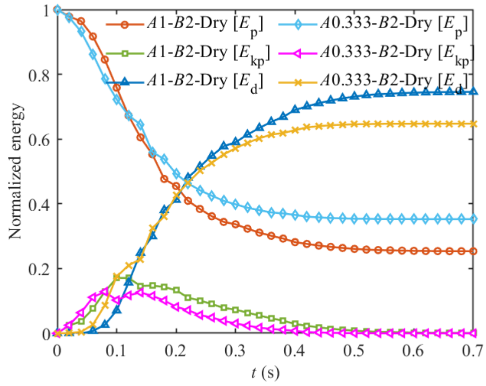

Fig. 8 Energy evolution during dry granular collapse of the cases $A1$-$B2$ and $A0.333$-B2

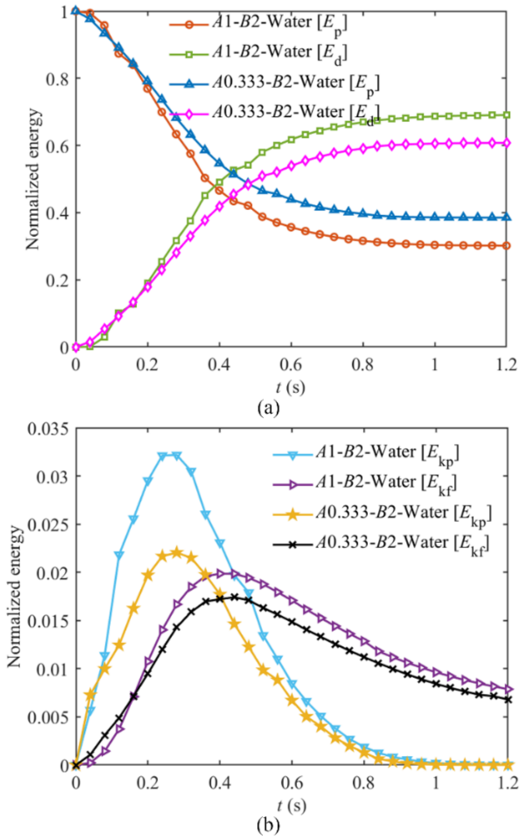

Fig. 9 Energy evolution during immersed granular collapse of the cases $A1$-$B2$ and $A0.333$-$B2$: (a) normalized gravitational potential energy and dissipated energy and (b) normalized particle kinetic energy and fluid kinetic energy

As can be seen from Fig. 6, at t = 0.1 s, all particles on the top-right corner of each granular column have collapsed to varying degrees. The particle velocity is large in the shallow part of the granular column and gradually decreases towards the interior part. In the bottom-left wedge area, the particle velocity is almost 0, indicating that there is a "static core" during the granular collapse. Moreover, the particle velocity of immersed case is significantly slower than that of dry case. As can be seen from Fig. 7, for the immersed granular collapse at t = 0.1 s, due to the drag by the collapsing particles within the sliding body (see the black curve in Fig. 7), the water body in this area also begins to move to the lower right and a vortex comes into being near the upper right of the sliding body. At this moment, the particle kinetic energy in the dry case is around the peak, and the gravitational potential energy decreases rapidly, along with the increasing rapidly dissipated energy (see Fig. 8). In terms of the immersed case, the particle kinetic energy is growing rapidly, and the fluid kinetic energy lags behind that of particles (see Fig. 9).

At t = 0.25 s, as can be seen from Fig. 6, for the dry case, the proportion of moving particles has reduced, and the particle velocity in the upper left part slows down obviously, leaving the particles in the shallow and front parts moving forward rapidly. Whereas, the proportion of moving particles in the immersed case has increased and the moving particles speed up notably. At this instant, the particle kinetic energy of dry collapse is in a gradually decreasing stage, and both the decreasing rate of gravitational potential energy and the increasing rate of dissipated energy gradually slow down (see Fig. 8). But now, the particle kinetic energy of immersed collapse is around the peak and the gravitational potential energy is rapidly decreasing, along with the rapidly increasing dissipated energy (see Fig. 9). Compared with the dry collapse, the current runout distance of the immersed collapse is obviously shorter and the deposit height is higher. Moreover, it can be seen from Fig. 7 that the fluid velocity within the sliding body area is faster and an obvious counterclockwise vortex is formed just outside the surface of sliding body. Under the combined action of downward collapse of the particles on the upper left, water obstruction on the right and vortex, a particular “bump” appears on the upper right corner of the immersed particles while the dry particles manifest a slightly concave surface (see Fig. 6).

As can be seen from Fig. 6, at t = 0.5 s, most particles in the dry collapse have stopped moving, and only a few particles in the surface layer and front move forward. For immersed collapse, there are still some particles moving but they are slowing down. Correspondingly, the various energies of the system in the dry collapse tends to be stable (see Fig. 8), while the underwater particle kinetic energy is in a gradually decreasing stage, with the decreasing rate of gravitational potential energy and the increasing rate of dissipated energy both slow down (see Fig. 9). At this instant, for the immersed collapse, the previously formed water vortex is propagating to the upper right (see Fig. 7), and the fluid kinetic energy gradually decreases after a peak that is smaller than the peak of particle kinetic energy (see Fig. 9). Moreover, it can be seen from Fig. 6 that the front of immersed particles is obviously thicker than that of dry particles.

As can be seen from Figs. 6-9, at t = 1.2 s, particles in all these cases have stopped moving, and the particle kinetic energy fades away. In terms of immersed collapse, the fluid velocity decreases obviously but its kinetic energy does not vanish at this instant, and the vortex continues to migrate further outside the particles surface. Finally, the particles surface of the dry case is concave, while the immersed particles present a gently humpy surface.

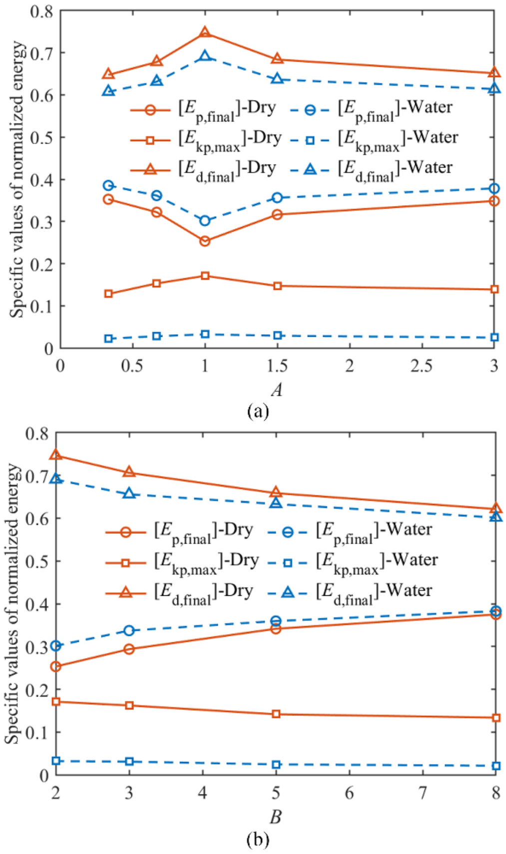

(a)

(b)

Fig. 10 Specific values of normalized energy for granular collapse: the effects of (a) particle aspect ratio and (b) particle blockiness

Through the above description, the process of granular collapse can be roughly divided into three stages, i.e., early collapse, transition and spread. The duration of each stage of immersed case is longer than that of dry case. In the early collapse stage, particles fall under gravity, and the gravitational potential energy is mainly converted to the kinetic energy of particles, with a delay of the dissipated energy. In this stage, for the dry collapse, compared with spherical particles, the upper non-spherical particles (initially random orientations) tend to an ordered orientation of "face-to-face contact", so the gravitational potential energy decreases slightly faster and the kinetic energy increases slightly faster (see Fig. 8). Correspondingly, at t = 0.1s, although the runout distance of the non-spherical particles is slightly shorter than that of spherical particles, but the upper part collapses slightly more (see Fig. 6). In the immersed case, due to the effects of the buoyancy and drag force of the water body, the above collapse feature of non-spherical particles is not obvious.

In the transition stage, the particles mainly transition from vertical collapse to horizontal spread, and the particle kinetic energy is around its peak, along with a sharp growth of dissipated energy. In this stage, compared with spherical particles, the decreasing rate of gravitational potential energy of non-spherical particles is slower and thus the kinetic energy is smaller. Moreover, the fluid kinetic energy of immersed non-spherical particle collapse is also smaller than that of immersed spherical particle collapse.

In the spread stage, the front and shallow particles move forward, and the particle velocity gradually decreases, along with a gradually decreasing particle kinetic energy. In this stage, compared with spherical particles, non-spherical particles have larger gravitational potential energy, smaller dissipated energy and kinetic energy, and the fluid kinetic energy for immersed case is also smaller.

Fig. 10 shows the variations of three specific values of normalized energy with the particle aspect ratio and particle blockiness, including the final gravitational potential energy $[E_{\mathrm{p,final}}]$, the maximum particle kinetic energy $[E_{\mathrm{kp,max}}]$ and the total dissipated energy $[E_{\mathrm{d,final}}]$. As can be seen from Fig. 10, under the same particle shape, the final gravitational potential energy of immersed collapse is higher and the maximum particle kinetic energy and total dissipated energy are lower than that of dry collapse. As can be seen from Fig. 10(a), as the particle aspect ratio deviates from 1, the final gravitational potential energy gradually increases, and the maximum kinetic energy and total dissipated energy both gradually decrease, regardless of dry or immersed case. As can be seen from Fig. 10(b), with the increase of particle blockiness, the final gravitational potential energy gradually increases, and the maximum particle kinetic energy and total dissipated energy gradually decrease, regardless of dry or immersed case. It can be seen from Fig. 5 and Fig. 10 that the final deposit height of granular collapse is closely correlated with the final gravitational potential energy, and the final runout distance is closely correlated with the maximum particle kinetic energy and total dissipated energy. Therefore, we can suggest that the motion and deposit characteristics of granular collapse are closely related to the transformation process of energy.

4.3 Particle interaction

In order to reveal the variation of particle interaction during the dry and immersed granular collapse with different particle shapes, the temporal evolution of coordination number and average contact normal force is respectively presented in Figs. 11 and 12. The coordination number *CN* indicates the average number of contacts around each particle, which can be obtained by dividing the sum of the contacts around each particle by the total number of particles. The average contact normal force $F_{\mathrm{n,av}}$ reflects the interaction intensity between particles, which can be calculated by dividing the sum of magnitude of each contact normal force by the total number of contacts. It should be noted that due to the particle Young's modulus in the numerical model being set lower than actual geomaterials, the average contact normal force values are restricted to demonstrating temporal evolution trends and comparing shape effects; their specific magnitudes may differ from physical measurements.

It can be seen from Figs. 11 and 12 that both coordination number and average contact normal force decrease sharply in the early collapse stage, no matter in dry or immersed case. During the transition stage, the coordination number and average contact normal force both fluctuate to some extent. In the spread stage, the

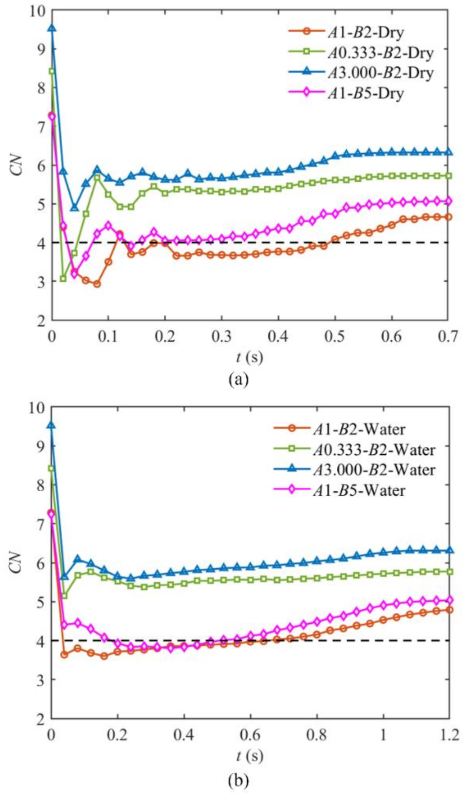

(a)

(b)

Fig. 11 Evolution of coordination number during (a) dry and (b) immersed granular collapse with different particle shapes

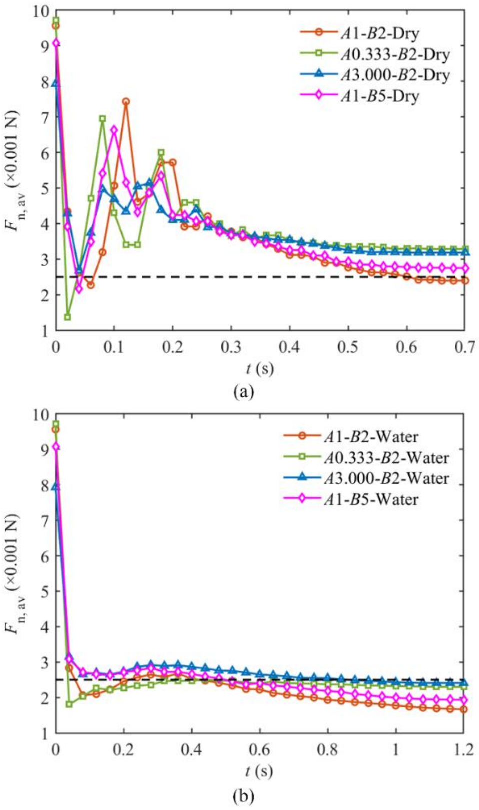

(a)

(b)

Fig. 12 Evolution of average contact normal force during (a) dry and (b) immersed granular collapse with different particle shapes coordination number gradually increases to a constant value and the average contact normal force gradually decreases to a constant value. The above variations of coordination number and average contact normal force shed light on the complex interaction mechanism between particles, including particle separation, collision, sliding and deposition during the granular collapse. It can also be seen from Figs. 11 and 12 that a more irregular particle shape results in a more larger coordination number and average contact normal force during the spread stage, indicating that there are more contacts and higher contact intensity between particles, and thus the interlocking and restraining effects between particles are stronger, thus reducing the fluidity and runout distance.

It is suggested that when the coordination number is less than 4, the granular system is unstable and liquefaction or fluidization occurs on a macro-scale (Gong *et al*. 2012). It can be inferred that the geometrically isotropic spherical particles *A*1-*B*2 and cubic particles *A*1-*B*5 are more likely to be fluidized in the transition stage (refer to the black dashed line in Fig. 11). It can be seen from Figs. 11 and 12 that, for the same particle shape, the coordination numbers in dry and immersed cases are nearly the same, but the average contact normal force between particles under water is smaller (see the black dashed line in Fig. 12 for reference), which mainly results from the buoyancy.

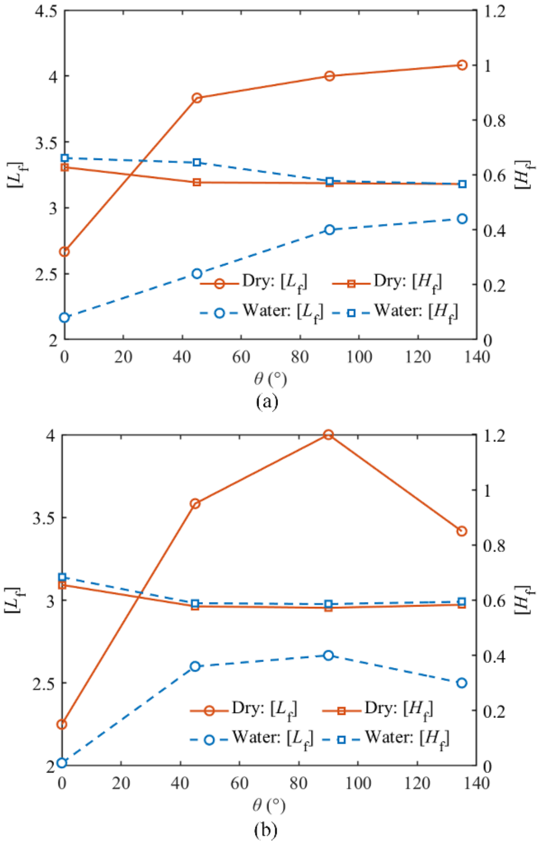

Fig. 13 Final runout distance and deposit height of granular collapse with different initial particle orientations respectively for (a) *A*0.333-*B*2 particles and (b) *A*3.000-*B*2 particles

5. The role of initial particle orientation

5.1 Final deposit geometry

The normalized final runout distance and deposit height of dry and immersed collapse with different main initial particle orientations θ are presented in Fig. 13 for platy ellipsoidal particles *A*0.333-*B*2 and elongated ellipsoidal particles *A*3.000-*B*2, respectively. As can be seen from Fig. 13, regardless of the initial particle orientation, the final runout distance of every immersed case is obviously smaller than that of corresponding dry case. With different initial particle orientations θ, the variation patterns of the final runout distance and deposit height are similar for the dry and immersed granular collapse. Specifically, for *A*0.333-*B*2 particles, the final runout distance increases with the increase of θ, with a maximum value at θ = 135°; for *A*3.000-*B*2 particles, the final runout distance first increases and then decreases with the increase of θ, with a maximum value at θ = 90°. The final deposit height is the highest at θ = 0°, and the difference among other three cases is little.

Figs. 5 and 13 demonstrate that regardless of particle shape or initial particle orientation, immersed collapses exhibit significantly different runout distances yet similar final deposition heights relative to their dry counterparts. As previously established in Sect. 4.2, fluid drag at the granular front substantially reduce immersed runout distance while potentially elevating deposit height. However, the counterclockwise vortex generated during immersed collapse (see Fig. 7) facilitates downward-right movement of particles in the upper-left region, resulting in a gently humpy surface and greater localized thickness than dry collapses. This mechanism conversely reduces overall deposit height. It is suggested that the two above counteracting effects collectively account for the minimal disparity in final deposit height between immersed and dry collapse cases.

By comparing Figs. 5 and 13, we can claim that, except for the sample with an initial particle orientation of 0°, the effect of initial particle orientation is smaller than that of particle shape, and the behavior caused by initial particle orientation is different for different particle shapes, that is, there is a complicated coupling effect between the initial particle orientation and particle shape.

5.2 Collapse dynamics

Taking the immersed granular collapse as an example, the motion characteristics and energy evolution of granular collapse with different initial particle orientations are analyzed, and the underlying physical mechanism of initial particle orientation effects is explored. Figs. 14 and 15 illustrate the particle translational velocity at 0.1 s, 0.25 s and 0.5 s of granular collapse with different initial particle orientations respectively for the case of *A*0.333-*B*2-Water and case of *A*3.000-*B*2-Water, and the temporal evolution of normalized energy are shown in Figs. 16 and 17, respectively.

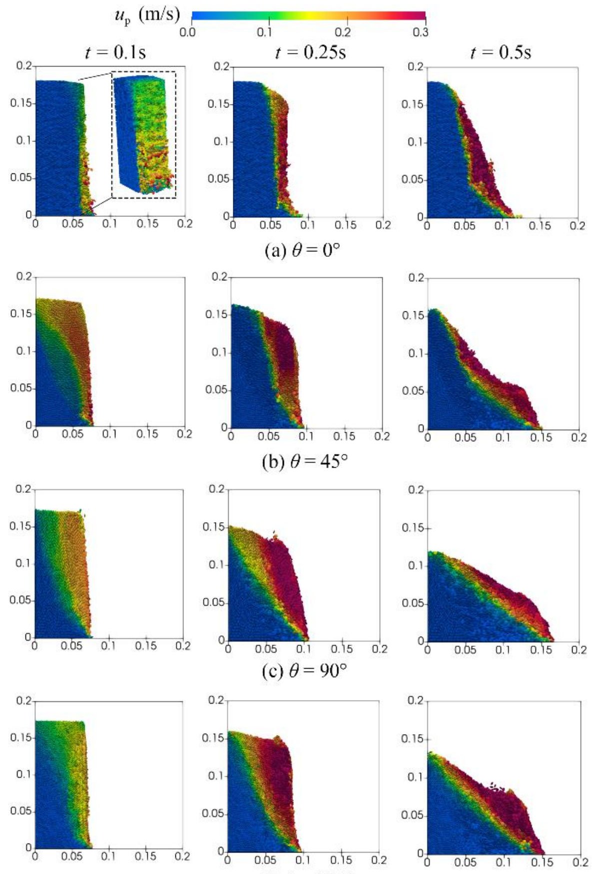

(a) $\theta = 0°$

(b) $\theta = 45°$

(c) $\theta = 90°$

(d) $\theta = 135°$

Fig. 14 Snapshots of the particle translational velocity for immersed collapse of *A*0.333-*B*2 particles with different initial particle orientations

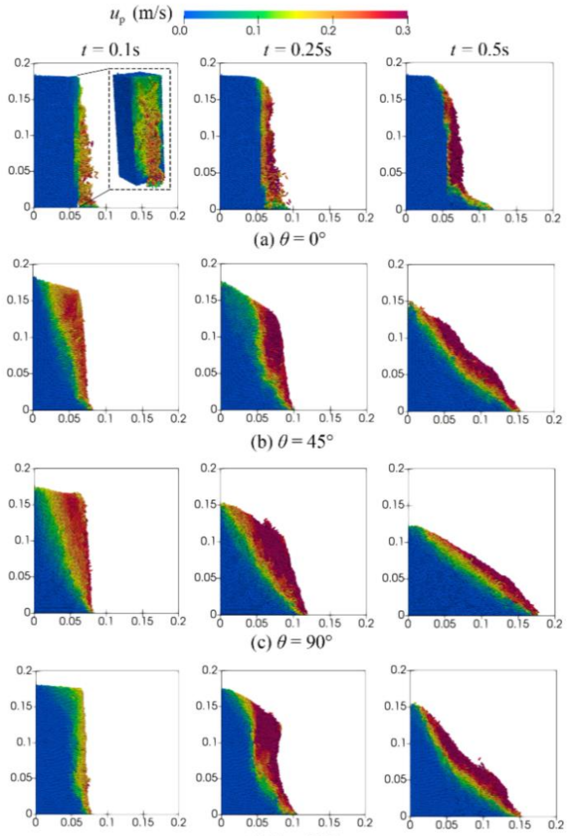

(a) $\theta = 0°$

(b) $\theta = 45°$

(c) $\theta = 90°$

(d) $\theta = 135°$

Fig. 15 Snapshots of the particle translational velocity for immersed collapse of *A*3.000-*B*2 particles with different initial particle orientations

It can be seen from Figs. 14 and 15 that the collapse mode of the granular column with an initial particle orientation of 0° is obviously different from that of the other three cases (θ = 45°, 90°, 135°). In the early stage, the whole structure formed by the particles oriented approximately horizontally is relatively stable and it is difficult to collapse under its own weight. However, due to the instantaneous deletion of the right baffle, some local particles on the right side of the granular column are extruded at t = 0.1 s. When t = 0.25 s, the upper right particles gradually slide down and deposit near the toe of the initial granular column together with the locally extruded particles. After t = 0.5 s, the local particle extrusion has stopped, and the upper particles continue to gradually collapse and heap up near the slope toe, which lasts for a long time before it stops completely. As can be seen from Figs. 16 and 17, the dissipated energy and the peak of particle kinetic energy of granular collapse with an initial particle orientation of 0° are much lower, and the gravitational potential energy is much higher. As a result, the granular collapse with an initial particle orientation of 0° produces the smallest final runout distance and the highest deposit height. Tapia-McClung (2012) and Coppin (2023) also pointed out that the fluidity is significantly reduced for elongated particles with their long axes nearly horizontally arranged.

As can be seen from Figs. 14 and 15, after the baffle is removed, at t = 0.1 s, the particles with an initial orientation of 45° (leaning on the right baffle) and the particles with an initial orientation of 90° (approximately upright) are prone to instability and tend to rotate clockwise, which results in the quick downward toppling of particles near the baffle. Whereas, in the granular column with an initial particle orientation of 135° (particles leaning on the left fixed wall), some particles near the free surface begin to slide out without obvious rotations. As a result, in the early collapse stage, compared with the particles with an initial orientation of 135°, the proportion of moving particles and the particle velocity are both larger for particles with an initial orientation of 45° and 90°, and their gravitational potential energy decreases faster, along with quickly increasing kinetic energy and dissipated energy (see Figs. 16 and 17).

As can be seen from Fig. 14 and Fig. 15, at t = 0.25 s, an obvious sliding plane is formed in each granular column with an initial particle orientation of 45°, 90° and 135°, and the particles in the sliding body speed up. At this moment, the particles in the upper left part have gradually stabilized for the granular collapse with an initial particle orientation of 45°, which makes the sliding plane steeper and the proportion of moving particles decreased, so the particle kinetic energy is lower than that of other two cases of θ = 90° and θ = 135° (see Figs. 16 and 17), which is quite evident for the particle shape of *A*0.333-*B*2.

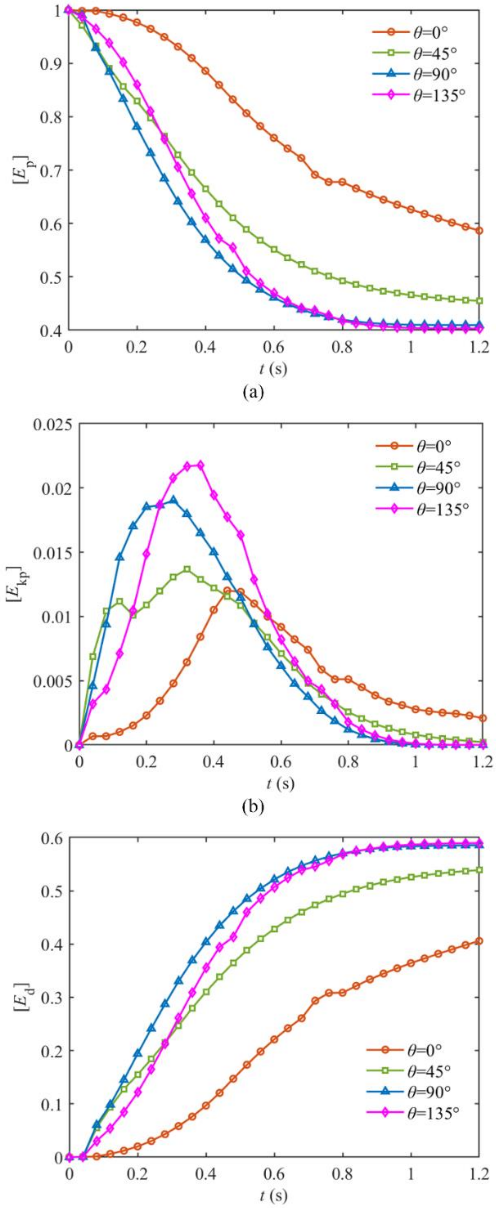

(a)

(b)

(c)

Fig. 16 Energy evolution for immersed collapse of *A*0.333-*B*2 particles with different initial particle orientations

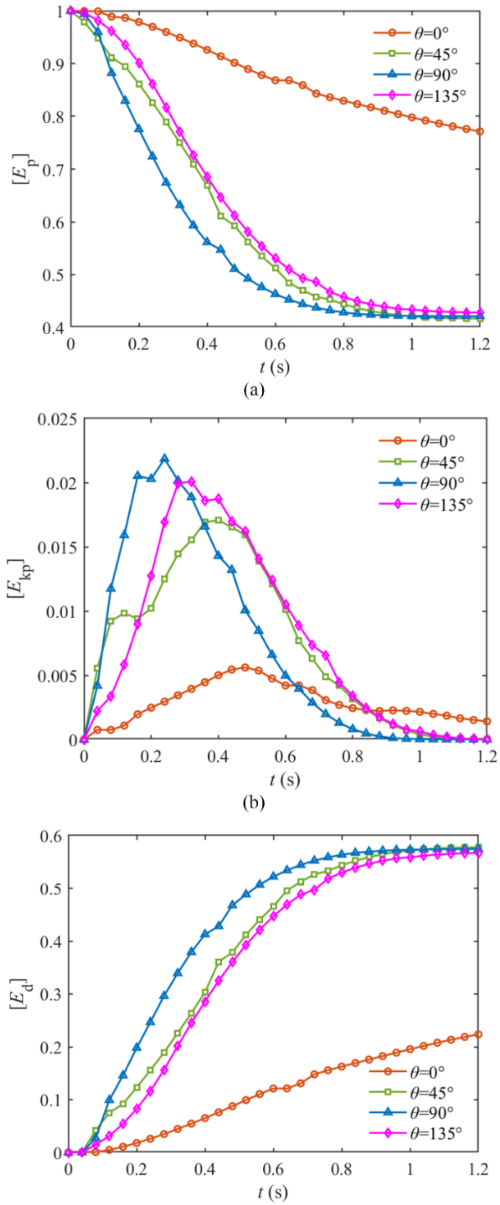

(a)

(b)

(c)

Fig. 17 Energy evolution for immersed collapse of *A*3.000-*B*2 particles with different initial particle orientations

As can be seen from Figs. 14-17, at t = 0.5 s, the proportion of moving particles has decreased in each granular collapse with an initial particle orientation of 45°, 90° and 135°, and the particle kinetic energy is also on the decline. At this moment, the particles with an initial orientation of 90° travel to the farthest distance and deposit to the lowest height, but the proportion of moving particles is already the least. The particles with an initial orientation of 135° have the largest proportion of moving particles and the fastest velocity, resulting in the largest particle kinetic energy. At the end, for *A*0.333-*B*2 particles, the runout distance of granular collapse with an initial orientation of 135° will exceed that of the case θ = 90°; however, for *A*3.000-*B*2 particles, the runout distance of the case θ = 90° is still the longest.

Compared Fig. 14(d) with Fig. 15(d), it can be found that at these three moments, compared with the elongated *A*3.000-*B*2 particles, the sliding plane in the platy *A*0.333-*B*2 particles is more gentle and deeper, with a higher proportion of moving particles and a larger peak value of particle kinetic energy. For *A*0.333-*B*2 particles, the peak kinetic energy is the highest when the initial orientation is 135° (see Fig. 16(b)). Whereas, for *A*3.000-*B*2 particles, the peak kinetic energy is the highest when the initial orientation is 90° (see Fig. 17(b)).

5.3 Particle orientation and contact

Next, taking the immersed collapse of granular columns composed of elongated ellipsoidal particles *A*3.000-*B*2 with

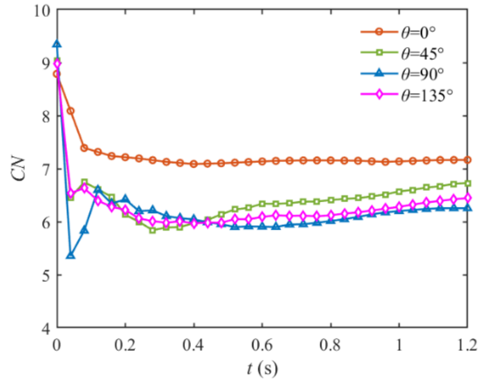

Fig. 18 Evolution of contact coordination number for immersed collapse of *A*3.000-*B*2 particles with different initial particle orientations

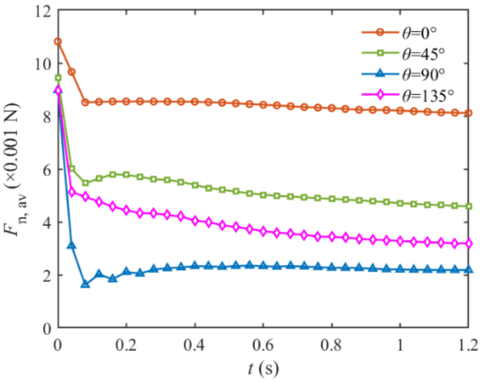

Fig. 19 Evolution of average contact normal force for immersed collapse of *A*3.000-*B*2 particles with different initial particle orientations

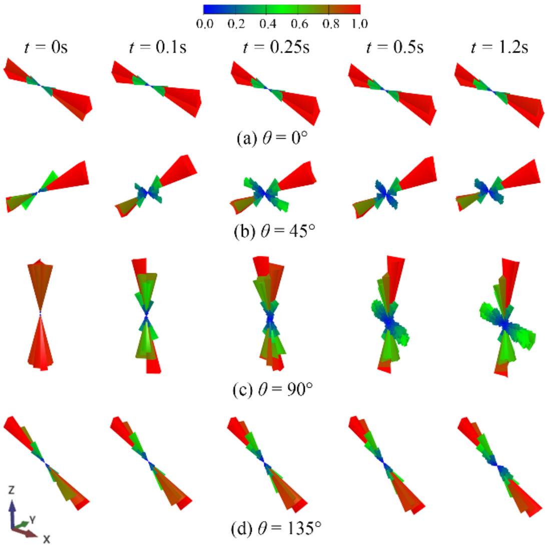

Fig. 20 Evolution of particle orientation distribution for immersed collapse of *A*3.000-*B*2 particles with different initial particle orientations

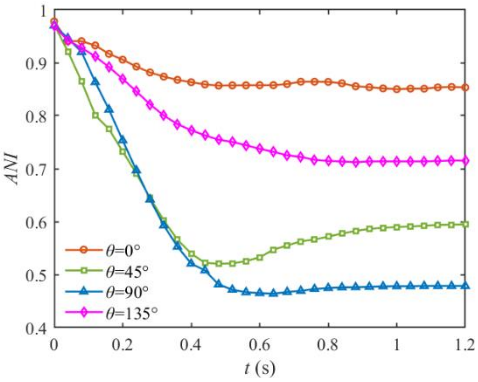

Fig. 21 Evolution of anisotropy coefficient of particle orientation distribution for immersed collapse of *A*3.000-*B*2 particles with different initial particle orientations

different initial particle orientations θ as an example, the evolution processes of the contact coordination number (Fig. 18), average contact normal force (Fig. 19) and particle orientation distribution (Figs. 20 and 21) are presented to further elucidate the influence of different initial particle orientations. Analogous microstructural evolution principles govern dry granular collapses and systems containing platy ellipsoidal particles *A*0.333-*B*2 for different initial particle orientations.

Figs. 18 and 19 show that both the contact coordination number and the average contact normal force undergo a developmental sequence characterized by rapid decrease, followed by oscillatory fluctuations, and eventual stabilization. Particles with an initial orientation of 0° exhibit minimal mobilization, and thus their coordination number and average contact normal force display the smallest magnitude of change. For particles initially oriented at 45°, significant rotation and sliding failure primarily occur within a localized subset of particles near the free surface within the upper-right part. The relatively limited extent of mobilized particles in this configuration results in a comparably smaller magnitude of reduction for both the coordination number and average contact normal force. Particles with initial orientations of 90° and 135° experience significantly greater mobilization throughout the collapse process, correlating with the comparably larger reductions observed in their respective coordination numbers and average contact normal forces.

The orientation of one *A*3.000-*B*2 particle n is characterized by the unit orientation vector s_n^i (the superscript i indicates the three components of the vector) parallel to its longest dimension. In Fig. 20, the extension length and color of each pyramid in three-dimensional space represent the number of particles within the corresponding orientation range, and these particle numbers are normalized using their maximum value. Fig. 21 shows the evolution of the anisotropy coefficient *ANI* for the particle orientation distribution, which can be obtained from the three principal values S_1, S_2, S_3 of the fabric tensor S_{ij} as follows

$$S_{ij} = \frac{1}{N_{\mathrm{p}}} \sum_{n=1}^{N_{\mathrm{p}}} s_n^i s_n^j \tag{19}$$

$$ANI = \frac{S_1 - S_3}{S_1 + S_2 + S_3} \tag{20}$$

As evident from Figs. 20 and 21, the initial directional alignment of particles within the column results in anisotropy coefficients approaching unity for all four configurations. After collapse, the degree of anisotropy decreases to varying extents due to particle rotation. Particles with initial orientations of 45° and 90° exhibit a more pronounced propensity for rotational instability (downward toppling). Consequently, their anisotropy coefficients diminish rapidly during the early collapse stage. Subsequently, in the transition stage, these partially rotated particles undergo realignment towards slope-parallel orientations, initiating sliding motion. This reorientation manifests as a transition from decreasing to gradually increasing anisotropy coefficients, ultimately stabilizing. Particles initially oriented at 0° demonstrate minimal anisotropy change, attributable to limited particle mobilization. Conversely, particles with an initial 135° orientation predominantly undergo progressive sliding with limited rotation. Their anisotropy coefficients therefore decrease monotonically to a stable value, which is notably lower than the final values observed for the 45° and 90° initial orientations.

To sum up, as can be inferred from the above results, in the early collapse stage dominated by particle falling, the particles with an initial orientation of 45° and 90° are more likely to downward toppling, which is conducive to the development of collapse. However, in the middle stage dominated by particle sliding, the particles with an initial inclination of 135° tend to slide more easily, which is also conducive to the development of collapse. Furthermore, considering the different particle shapes, the platy *A*0.333-*B*2 particles are prone to sliding, so the final runout distance is the longest for the particles with an initial orientation of 135°; the elongated *A*3.000-*B*2 particles are easier to toppling, so the final runout distance is the longest for the particles with an initial orientation of 90°.

6. Conclusions

In this study, based on the superquadric DEM and the coupled CFD-DEM, the dry and immersed collapse process of granular columns with different particle shapes (aspect ratio and blockiness) and different initial particle orientations were simulated. The effects of particle shape and initial particle orientation on the collapse dynamics and final deposit geometry were investigated, and the underlying physical mechanisms of the influence of these two factors were explored. The main conclusions extracted from the results are depicted as follows:

- Compared with the dry granular collapse, the duration of immersed granular collapse is significantly increased and the final runout distance is obviously reduced. However, the variation patterns of the final runout distance and deposit height with the particle shape and initial particle orientation are similar for both dry and immersed granular collapse.
- In terms of the effect of particle aspect ratio A, from the turning point $A = 1$ (spherical) to both sides, the collapse of particles with larger A (elongated) or smaller A (platy) results in a shorter final runout distance and a higher final deposit height, along with a higher final gravitational potential energy and lower maximum particle kinetic energy and total dissipated energy.
- With the increase of particle blockiness B (more angular), the final gravitational potential energy of granular collapse increases, and the maximum particle kinetic energy and total dissipated energy both decrease, resulting in a shorter final runout distance and a higher final deposit height.
- A more irregular particle shape results in more larger coordination number and average contact normal force during the spread stage of granular collapse, suggesting more contacts and higher contact intensity between particles, and thus the interlocking and restraining effects between particles are stronger, thus reducing the particle fluidity and final runout distance.
- In terms of the effect of main initial particle orientation θ, the collapse of particles with $\theta = 0°$ (approximately horizontal) produces an obviously smaller final runout distance, and progresses in a particular way that some particles being first squeezed out from the lateral free surface followed by the gradual slide of particles in the upper parts.
- There is a complicated coupling effect between the initial particle orientation and particle shape. For platy ellipsoidal particles, the collapse of particles with $\theta = 135°$ (leaning on the fixed wall) generates the longest final runout distance, because this initial orientation is conducive to the outward sliding of platy particles. Whereas, for elongated ellipsoidal particles, the collapse of particles with $\theta = 90°$ (approximately upright) generates the longest final runout distance, because this initial orientation is conducive to the downward toppling of elongated particles.

It should be noted that the granular columns in this study were constructed with an aspect ratio of 3. This specific column aspect ratio was deliberately selected as it represents an intermediate column height that effectively captures both inertial and frictional regimes while maintaining computational efficiency. However, given the well-documented sensitivity of granular collapse to initial column geometry, future investigations should systematically examine how the observed effects of particle shape and initial particle orientation manifest across a broader range of column aspect ratios.

Acknowledgments

The authors are very grateful to several developers of MFiX in NETL of the United States for their valuable guidance in the use of the software. This work is supported by the National Natural Science Foundation of China (Grant Nos. 52079067, 51879142).

References

Adesina, P., O'Sullivan, C. and Wang, T. (2024), “DEM study on the effect of particle shape on the shear behaviour of granular materials”, *Comp. Part. Mech.*, **11**(1), 447-466. https://doi.org/10.1007/s40571-023-00632-8.

Bao, X., Wu, H., Xiong, H. and Chen, X. (2023), "Particle shape effects on submarine landslides via CFD-DEM", *Ocean Eng.*, **284**, 115140. https://doi.org/10.1016/j.oceaneng.2023.115140.

Bougouin, A., Lacaze, L. and Bonometti, T. (2019), "Collapse of a liquid-saturated granular column on a horizontal plane", *Phys. Rev. Fluids*, **4**(12), 124306. https://doi.org/10.1103/PhysRevFluids.4.124306.

Cabrera, M. and Estrada, N. (2019), "Granular column collapse: Analysis of grain-size effects", *Phys. Rev. E*, **99**, 012905. https://doi.org/10.1103/PhysRevE.99.012905.

Chen, S., Xu, W. and Zhang, G. (2024), "Numerical simulation of potential impulse waves generated by the Mogu rock landslide at varying water levels in the Lianghekou Reservoir, China", *Landslides*, **21**, 2289-2305. https://doi.org/10.1007/s10346-024-02286-w.

Coppin, N., Henry, M., Cabrera, M., Azéma, E., Dubois, F., Legat, V. and Lambrechts, J. (2023), "Collapse dynamics of two-dimensional dry and immersed granular columns of elongated grains", *Phys. Rev. Fluids*., **8**(9), 094303. https://doi.org/10.1103/PhysRevFluids.8.094303.

Crosta, G., Imposimato, S. and Roddeman, D. (2009), "Numerical modeling of 2-D granular step collapse on erodible and nonerodible surface", *J. Geophys. Res-Earth*., **114**, F03020. https://doi.org/10.1029/2008JF001186.

Cui, W., Wei, J., Wang, C., Wang, X. and Zhang, S. (2021), "Discrete element simulation of collapse characteristics of particle column considering gradation and shape", *Chinese J. Geotech. Eng.*, **43**(12), 2230-2239. https://doi.org/10.11779/CJGE202112009.

Di Felice, R. (1994), "The voidage function for fluid-particle interaction systems", *Int. J. Multiphas. Flow*, **20**(1), 153-159. https://doi.org/10.1016/0301-9322(94)90011-6.

Dong, T., Zheng, Y., Liang, K. and Liu, C. (2022), "Shear strength and shear bands of anisotropic sand", *Acta Geotech.*, **17**(7), 2841-2853. https://doi.org/10.1007/s11440-021-01372-w.

Fan, Y., Wang, F. and Zhang, F. (2024), "Research on dynamic characteristics of granular flow based on the material point method", *Comp. Part. Mech*., **11**(3), 1021-1034. https://doi.org/10.1007/s40571-023-00670-2.

Fu, P. and Dafalias, Y.F. (2011), "Study of anisotropic shear strength of granular materials using DEM simulation", *Int. J. Numer. Anal. Meth. Geomech*., **35**(10), 1098-1126. https://doi.org/10.1002/nag.945.

Ganser, G.H. (1993), "A rational approach to drag prediction of spherical and nonspherical particles", *Powder Technol.*, **77**(2), 143-152. https://doi.org/10.1016/0032-5910(93)80051-B.

Gao, X., Yu, J., Lu, L.Q., Li, C. and Rogers, W.A. (2021), "Development and validation of SuperDEM-CFD coupled model for simulating non-spherical particles hydrodynamics in fluidized beds", *Chem. Eng. J.*, **420**, 127654. https://doi.org/10.1016/j.cej.2020.127654.

Gao, X., Yu, J., Portal, R.J.F., Dietiker, J.F., Shahnam, M. and Rogers, W.A. (2022), "Development and validation of SuperDEM for non-spherical particulate systems using a superquadric particle method", *Particuology*, **61**, 74-90. https://doi.org/10.1016/j.partic.2020.11.007.

Gong, G.B., Thornton, C. and Chan, A.H.C. (2012), "DEM simulations of undrained triaxial behavior of granular material", *J. Eng. Mech.*, **138**(6), 560-566. https://doi.org/10.1061/(ASCE)EM.1943-7889.0000366.

Gong, J., Cheng, L., Liu, M., Jiang, J. and Ou, X. (2024), "The effect of particle shape on the collapse characteristics of granular columns via the DEM", *Adv. Powder Technol.*, **35**(1), 104283. https://doi.org/10.1016/j.apt.2023.104283.

Gong, J., Cheng, L., Zhao, L., Zou, J., Li, L. and Nie, Z. (2021), "Study on the packing and shear characteristics of granular mixtures via the DEM", *Geomech. Eng.*, **27**(3), 223-237. https://doi.org/10.12989/gae.2021.27.3.223.

Guo, X., Stoesser, T., Zheng, D., Luo, Q., Liu, X. and Nian, T. (2023), "A methodology to predict the run-out distance of submarine landslides", *Comput. Geotech.*, **153**, 105073. https://doi.org/10.1016/j.compgeo.2022.105073.

Hoang, U.T. and Nguyen, N.H.T. (2023), "Particle shape effects on granular column collapse using superquadric DEM", *Powder Technol.*, **424**, 118559. https://doi.org/10.1016/j.powtec.2023.118559.

Hözer, A. and Sommerfeld, M. (2008), "New simple correlation formula for the drag coefficient of non-spherical particles", *Powder Technol.*, **184**(3), 361-365. https://doi.org/10.1016/j.powtec.2007.08.021.

Jing, L., Yang, G.C., Kwok, C.Y. and Sobral Y.D. (2018), "Dynamics and scaling laws of underwater granular collapse with varying aspect ratios", *Phys. Rev. E*, **98**(4), 042901. https://doi.org/10.1103/PhysRevE.98.042901.

Kermani, E. and Qiu, T. (2020), "Simulation of quasi-static axisymmetric collapse of granular columns using smoothed particle hydrodynamics and discrete element methods", *Acta Geotech.*, **15**(2), 423-437. https://doi.org/10.1007/s11440-018-0707-9.

Kermani, E., Qiu, T. and Li, T. (2015), "Simulation of collapse of granular columns using the discrete element method", *Int. J. Geomech.*, **15**(6), 04015004. https://doi.org/10.1061/(ASCE)GM.1943-5622.0000467.

Kumar, K., Delenne, J.Y. and Soga, K. (2017), "Mechanics of granular column collapse in fluid at varying slope angles", *J. Hydrodyn.*, **29**(4), 529-541. https://doi.org/10.1016/S1001-6058(16)60766-7.

Lai, Z., Jiang, E., Zhao, L., Wang, Z., Wang, Y. and Li, J. (2023), "Granular column collapse: Analysis of inter-particle friction effects", *Powder Technol.*, **415**, 118171. https://doi.org/10.1016/j.powtec.2022.118171.

Lube, G., Huppert, H.E., Sparks, R.S.J. and Freundt, A. (2005), "Collapses of two-dimensional granular columns", *Phys. Rev. E*, **72**(4), 041301. https://doi.org/10.1103/PhysRevE.72.041301.

Polanía, O., Cabrera, M., Renouf, M. and Azéma, E. (2022), "Collapse of dry and immersed polydisperse granular columns: A unified runout description", *Phys. Rev. Fluids*, **7**(8), 084304. https://doi.org/10.1103/PhysRevFluids.7.084304.

Rondon, L., Pouliquen, O. and Aussillous, P. (2011), "Granular collapse in a fluid: Role of the initial volume fraction", *Phys. Fluids*, **23**(7), 073301. https://doi.org/10.1063/1.3594200.

Soltanbeigi, B., Podlozhnyuk, A., Papanicolopulos, S.A., Kloss, C., Pirker, S. and Ooi, J.Y. (2018), "DEM study of mechanical characteristics of multi-spherical and superquadric particles at micro and macro scales", *Powder Technol.*, **329**, 288-303. https://doi.org/10.1016/j.powtec.2018.01.082.

Sun, Y., Zhang, W., Wang, X. and Liu, Q. (2020), "Numerical study on immersed granular collapse in viscous regime by particle-scale simulation", *Phys. Fluids*, **32**(7), 073313. https://doi.org/10.1063/5.0015110.

Tapia-McClung, H. and Zenit, R. (2012), "Computer simulations of the collapse of columns formed by elongated grains", *Phys. Rev. E*, **85**(6), 061304. https://doi.org/10.1103/PhysRevE.85.061304.

Trepanier, M. and Franklin, S.V. (2010), "Column collapse of granular rods", *Phys. Rev. E*, **82**(1), 011308. https://doi.org/10.1103/PhysRevE.82.011308.

Wang, Y., Zhou, L., Wu, Y. and Yang, Q. (2018), "New simple correlation formula for the drag coefficient of calcareous sand particles of highly irregular shape", *Powder Technol.*, **326**, 379-392. https://doi.org/10.1016/j.powtec.2017.12.004.

Wedel, J., Strakl, M., Hribersek, M., Steinmann, P. and Ravnik, J. (2024), "A novel particle–particle and particle–wall collision model for superellipsoidal particles", *Comp. Part. Mech.*, **11**(1), 211-234. https://doi.org/10.1007/s40571-023-00618-6.

Xing, L., Wang, G. and Gong, W. (2025), “Model tests of the failure behaviors of buildings under the impact of granular flow”, *Landslides*, **22**, 373-392. https://doi.org/10.1007/s10346-024-02372-z.

Xu, W., Dong, X. and Ding. W. (2019), “Analysis of fluid-particle interaction in granular materials using coupled SPH-DEM method”, *Powder Technol.*, **353**, 459-472. https://doi.org/10.1016/j.powtec.2019.05.052.

Yang, G., Jing, L., Kwok, C.Y. and Sobral, Y.D. (2019) “A comprehensive parametric study of LBM-DEM for immersed granular flows”, *Comput. Geotech.*, **114**, 103100. https://doi.org/10.1016/j.compgeo.2019.103100.

Zhang, B., Li, W., Pu, J., Bi, Y. and Huang, Y. (2024), “Centrifuge and DEM investigation of dry granular impacts: Effect of granular volume under high-speed impact conditions”, *Landslides*, **21**, 1439-1459. https://doi.org/10.1007/s10346-024-02219-7.

Zhang, W.Y. and Askarinejad, A. (2021), “Ultimate lateral pressures exerted on buried pipelines by the initiation of submarine landslides”, *Landslides*, **18**, 3337-3351. https://doi.org/ 10.1007/s10346-021-01711-8.

Zhang, X., Krabbenhoft, K., Sheng, D. and Li, W. (2015), “Numerical simulation of a flow-like landslide using the particle finite element method”, *Comput. Mech.*, **55**, 167-177. https://doi.org/10.1007/s00466-014-1088-z.

Zhao, Y., Xu, L., Umbanhowar, P.B. and Lueptow, R.M. (2019), “Discrete element simulation of cylindrical particles using super-ellipsoids”, *Particuology*, **46**, 55-66. https://doi.org/10.1016/j.partic.2018.04.007.

CC